Origin of the multiple charge density wave order in $1T$-VSe_2

J. G. Si,[1,2] W. J. Lu,[1,*] H. Y. Wu,[3] H. Y. Lv,[1] X. Liang,[1,2] Q. J. Li,[4] and Y. P. Sun[1,5,6,†]

[1]*Key Laboratory of Materials Physics, Institute of Solid State Physics, Chinese Academy of Sciences, Hefei 230031, China*

[2]*University of Science and Technology of China, Hefei 230026, China*

[3]*Institutes of Physical Science and Information Technology, Anhui University, Hefei 230601, China*

[4]*State Key Laboratory of Superhard Materials, Jilin University, Changchun 130012, China*

[5]*High Magnetic Field Laboratory, Chinese Academy of Sciences, Hefei 230031, China*

[6]*Collaborative Innovation Center of Microstructures, Nanjing University, Nanjing 210093, China*

(Received 2 January 2020; revised manuscript received 17 May 2020; accepted 20 May 2020; published 1 June 2020)

Transition-metal dichalcogenide $1T$-VSe_2 experimentally exhibits multiple charge density wave (CDW) orders, but its origin is still under debate. Using first-principles calculations, we investigate the origin of CDW orders in $1T$-VSe_2 and clarify the ground state of CDW in the freestanding monolayer. Our results show that both Fermi-surface nesting and electron-phonon coupling account for the $4 \times 4 \times 3$ CDW superstructure in bulk $1T$-VSe_2, while the momentum-dependent electron-phonon coupling-induced $\sqrt{7} \times \sqrt{3}$ CDW superstructure is most stable in the freestanding monolayer $1T$-VSe_2. For monolayer $1T$-VSe_2, the substrate-induced compressive strain can turn the ground state into the 4×4 CDW superstructure, while tensile strain preserves the $\sqrt{7} \times \sqrt{3}$ superstructure. Our results demonstrate the origin of the CDW orders in $1T$-VSe_2 and shed light on the experimental observation of multiple CDW orders in monolayer $1T$-VSe_2.

DOI: 10.1103/PhysRevB.101.235405

I. INTRODUCTION

Since graphene was successfully exfoliated in 2004, many fascinating properties have made it turn into one of the most popular materials, stimulating the search for more two-dimensional (2D) materials [1,2]. Among 2D materials, transition-metal dichalcogenides (TMDCs) display a multitude of correlation effects that encompass diverse physical and chemical properties [3–7], such as the charge density wave (CDW), superconducting state, Weyl semimetal state, magnetic ordering, and so on, attracting widespread attention.

CDW is a collective phenomenon accompanied by inherent modulation of electron density and associated periodic lattice distortion, which is a very pronounced phenomenon widely studied in TMDCs and has potential applications, such as oscillators and memory devices [8–11]. It is an old but longstanding issue with regard to the origin of CDW formation [12–20]. The mechanism of the CDW in TMDCs was initially explained by Fermi-surface nesting, which drives charge redistribution accompanied by a periodic lattice distortion [12–14]. Some research groups argued that the charge density redistribution is driven by momentum-dependent electron-phonon coupling (EPC)-induced periodic lattice distortion, where Fermi-surface nesting is negligible [15–17,21]. There are some research groups that used the combination of electron-phonon matrix elements and the bare response function to explain the formation of the CDW [22]. It turns out that this method is very effective for $2H$-$NbSe_2$ and bulk $1T$-VSe_2 [23,24]. Exciton condensation (electron-hole coupling) that was proposed a long time ago [25–28] was theoretically regarded as another mechanism of the CDW formation [18,19,29–31] and was recently detected in $1T$-$TiSe_2$ [29,30]. The origin of CDW still needs to be clarified for different systems.

Among TMDCs, $1T$-VSe_2 is a resurgent material with multiple CDW orders in monolayer form, which displays distinctly different properties from the bulk. Bulk $1T$-VSe_2 is metallic with strong intralayer coupling due to V-Se covalent and the weak interlayer van der Waals interaction. It undergoes a CDW transition around 110 K, forming a three-dimensional CDW superstructure ($4 \times 4 \times 3$) with the CDW wave vector $Q_{CDW} = 0.25a^* + 0.3c^*$ [32,33]. Due to the improvement in the preparation process, $1T$-VSe_2 can be prepared into thin films or a monolayer. Bonilla *et al.* used molecular beam epitaxy (MBE) to grow monolayer $1T$-VSe_2 on graphite (highly oriented pyrolytic graphite) and MoS_2 substrates and found strong ferromagnetic order, which is contrary to the bulk one [34]. Chen *et al.* grew a $1T$-VSe_2 monolayer on bilayer graphene using MBE and found a $\sqrt{7} \times \sqrt{3}$ CDW superstructure with no ferromagnetic exchange splitting [35]. Recently, the ferromagnetism of monolayer $1T$-VSe_2 was explained by the Se-defect-induced magnetic order [36]. In addition, other CDW orders in monolayer or few-layer $1T$-VSe_2 on different substrates have also been observed experimentally, such as the 4×4 CDW order below 140 K [37,38] and the $2 \times \sqrt{3}$ and $4 \times \sqrt{3}$ CDW orders with transition temperatures of 350 and 100 K, respectively [39,40]. It can be seen that the CDW order in monolayer $1T$-VSe_2 is strongly dependent on preparation conditions and is still controversial. We can see that the CDW orders of

*wjlu@issp.ac.cn
†ypsun@issp.ac.cn

monolayer $1T$-VSe_2 are quite different from that of the bulk form, which is unlike the cases of $1T$-TaX_2 (X = S, Se) and $1T$-$TiSe_2$ [41–47]. The puzzling ground state of CDW in monolayer $1T$-VSe_2 and the real physical mechanism still need to be clarified.

In this work, we investigate the multiple CDW orders in $1T$-VSe_2 with the freestanding form and substrate-induced strain by using first-principles calculations. We find that the origin of the CDW in monolayer $1T$-VSe_2 is dominated by the EPC, different from the case of bulk $1T$-VSe_2, for which both Fermi-surface nesting and EPC play significant roles in the origin of the three-dimensional $4 \times 4 \times 3$ CDW superstructure. Our results show that the $\sqrt{7} \times \sqrt{3}$ CDW superstructure is the most stable in freestanding monolayer $1T$-VSe_2. By simulating the substrate-induced strain, we find that the compressive strain can turn the CDW ground state ($\sqrt{7} \times \sqrt{3}$) into the 4×4 superstructure, while the tensile strain can preserve the $\sqrt{7} \times \sqrt{3}$ one. Our observations clarify the origin of CDW order in $1T$-VSe_2 and confirm the ground state of CDW in monolayer $1T$-VSe_2.

II. COMPUTATIONAL DETAILS

The first-principles calculations were carried out with the QUANTUM ESPRESSO package based on density functional theory (DFT) [48]. The ultrasoft pseudopotentials were used to describe the interaction between electrons and ionic cores [49]. The exchange-correlation interaction was treated by the generalized gradient approximation, which is parameterized by the Perdew-Burke-Ernzerhof functional [50]. In order to obtain accurate structural parameters of bulk $1T$-VSe_2, the semiempirical DFT-D2 method was induced to treat the interlayer van der Waals interaction [51]. The energy cutoff of the wave functions (charge density) was set to be 60 (600) Ry. The Gaussian smearing method with a smearing parameter of $\sigma = 0.01$ Ry was used. All structures were fully relaxed until the Hellmann-Feynman force acting on each atom was less than 10^{-4} Ry/Å, and the convergence criterion for self-consistent calculations was set to be 10^{-6} Ry. In order to simulate the case of a monolayer, an 18-Å vacuum layer was introduced to prevent interlayer interaction. Phonon dispersion curves of the normal state were calculated based on density functional perturbation theory [52], where a $24 \times 24 \times 16$ ($32 \times 32 \times 1$) k-point grid and a $6 \times 6 \times 4$ ($8 \times 8 \times 1$) q-point grid were used for the bulk (monolayer) form. The substrate-induced strain was simulated by changing the lattice parameters. The magnitude of the strain was defined as $\varepsilon = (a - a_0)/a_0 \times 100\%$, where positive (negative) values of ε indicate that the biaxial tensile (compressive) strain is applied to the system.

III. RESULTS AND DISCUSSION

Bulk $1T$-VSe_2 has a layered structure with space group $P = \bar{3}m1$, which has one V atom and two Se atoms located at (0,0,0) and $(1/3, 2/3, \pm z)$ sites, respectively. The adjacent layers are held together by van der Waals forces, and each V atom is surrounded by the nearest six Se atoms, constituting an octahedron structure, as illustrated in Fig. 1(a). The optimized lattice constants of a and c are 3.356 and 6.105 Å, respectively, consistent with the previous experimental reports [40]. The band structure of bulk $1T$-VSe_2 shows a classical band characteristic of TMDCs with a $1T$ phase, and only one band crosses the Fermi level (see Fig. SI in the Supplemental Material [53]). The calculated Fermi surface is shown in Fig. 1(b), which is consistent with the previous reports [37,54].

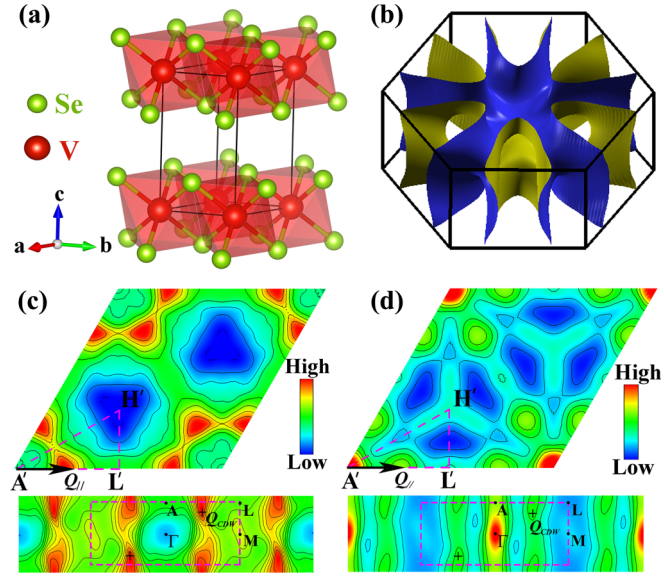

FIG. 1. (a) Crystal structure of bulk $1T$-VSe_2. The red (green) balls represent V (Se) atoms. (b) Fermi surface of bulk $1T$-VSe_2. (c) Real and (d) imaginary parts of the electron susceptibility cross section in the plane of $q_z = \frac{1}{3}c^*$, and the corresponding maximum is marked by $Q_{//}$. The bottom panels in (c) and (d) are the real and imaginary parts of electron susceptibility along the $+k_z$ (ΓA) direction, where Q_{CDW} is indicated by the crosses.

Fermi-surface nesting is always responsible for the origin of CDW in early reports [12–14] and can be evaluated quantitatively by calculating electron susceptibility [14]. The nesting function is the low-frequency limit of the imaginary part of the bare electronic susceptibility under constant matrix element approximation, while the real part of the electronic susceptibility determines the stability of the electronic system. Therefore, if the CDW order is induced by Fermi-surface nesting, both the real and imaginary parts of the electronic susceptibility should peak at the Q_{CDW} [14]. The real part of the electron susceptibility χ' is defined as

$$\chi'(q) = \sum_k \frac{f(\varepsilon_k) - f(\varepsilon_{k+q})}{\varepsilon_k - \varepsilon_{k+q}}, \tag{1}$$

where $f(\varepsilon_k)$ is the Fermi-Dirac distribution function. The imaginary part of the electron susceptibility χ'' can be calculated by

$$\chi''(q) = \sum_k \delta(\varepsilon_k - \varepsilon_F)\delta(\varepsilon_{k+q} - \varepsilon_F). \tag{2}$$

For bulk $1T$-VSe_2, we used a dense $40 \times 40 \times 30$ k-point grid for calculating eigenvalues to further derive the electron susceptibilities. Figure 1(c) shows the real part of the electron susceptibility cross section at the plane of $q_z = \frac{1}{3}c^*$, and we defined the top 5% of the real part of the electron susceptibility as the maximum, which is labeled by $Q_{//}$. The imaginary

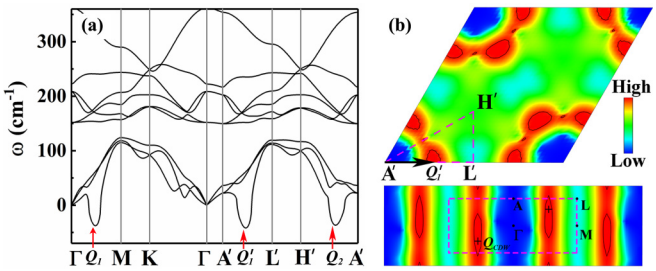

FIG. 2. (a) Phonon dispersion curves of bulk $1T$-VSe_2, where Q_1, Q_1', and Q_2 stand for the prominent imaginary frequencies. (b) Phonon linewidth of the lowest phonon mode of bulk $1T$-VSe_2 in the $q_z = \frac{1}{3}c^*$ plane (top) and along the $+k_z$ (ΓA) direction (bottom).

part of the electron susceptibility cross section at the plane of $q_z = \frac{1}{3}c^*$ is shown in Fig. 1(d). Since the imaginary part of the electron susceptibility always shows the maximum around the zero point, which is due to intraband contributions from a weakly dispersing band and is irrelevant for the nesting [55], we labeled the second maximum as $Q_{//}$. It can be seen that both the χ' and χ'' maxima locate at the same position of $Q_{//} = \frac{1}{2}\Gamma M = \frac{1}{4}a^*$, which agrees well with the projection of Q_{CDW} in the plane of $q_z = \frac{1}{3}c^*$. We also plotted the electron susceptibility along the k_z direction, as shown in the bottom panels of Figs. 1(c) and 1(d). We can see that the positions of Q_{CDW} show maximum values of the electron susceptibility, as marked by the crosses.

The phonon dispersion curves of bulk $1T$-VSe_2 are calculated as shown in Fig. 2(a), where high-symmetry points A', L', and H' in the $q_z = \frac{1}{3}c^*$ plane correspond to the Γ, M, and K points in the $q_z = 0$ plane, agreeing well with a previous report [40]. For CDW materials, the calculation of the phonon spectrum has proved to be an effective method to describe the CDW instability [42,47]. We find three remarkably soft phonon modes. Q_1 and Q_1' have the same composition ($\frac{1}{4}a^*$) projected in the in-plane section, standing for the in-plane part of the $4 \times 4 \times 3$ CDW superstructure in real space. The softened mode Q_2 is responsible for the $4 \times \sqrt{3}$ CDW superstructure reported by Zhang *et al.* [40]. We also calculated the phonon linewidth γ that is directly related to the EPC since the large EPC may induce lattice distortion and a consequent CDW [15,16,41]. Here, γ is defined as

$$\gamma_{qv} = 2\pi\omega_{qv} \sum_{ij} \int \frac{d^3k}{\Omega_{BZ}} |g_{qv}(k,i,j)|^2 \times \delta(\varepsilon_{q,i} - \varepsilon_F)\delta(\varepsilon_{k+q,j} - \varepsilon_F). \quad (3)$$

Here, $g_{qv}(k,i,j)$ is the EPC coefficient and can be calculated by

$$g_{qv}(k,i,j) = \left(\frac{\hbar}{2M\omega_{qv}}\right)^{1/2} \langle \psi_{i,k} | \frac{dV_{\mathrm{SCF}}}{d\hat{u}_{qv}} \hat{\xi}_{qv} | \psi_{j,k+q} \rangle, \quad (4)$$

where ψ is the wave function, V_{SCF} is the Kohn-Sham potential, $\hat{u}$ is atomic displacement, and $\hat{\xi}$ is the phonon eigenvector. It can be deduced from Eq. (3) that γ reflects the strength of the EPC, which does not depend on the real or imaginary nature of the phonon frequency [17,41]. The top panel of Fig. 2(b) shows the calculated phonon linewidth of the lowest phonon mode in the $q_z = \frac{1}{3}c^*$ plane. The contours are plotted by considering the top 5% of the phonon linewidth, which is defined as the maximum and located at $\frac{1}{4}a^*$. The phonon linewidth along the q_z direction is shown in the bottom panel of Fig. 2(b), and we find that Q_{CDW} is in the area with the maximum. One can see that the maximum of γ is very consistent with Q_{CDW}. Therefore, we consider that both Fermi-surface nesting and the EPC account for the origin of the $4 \times 4 \times 3$ CDW superstructure in bulk $1T$-VSe_2, which was also suggested previously [39,40,54].

TABLE I. Lattice vectors of CDW structures in real space and reciprocal space as a function of the lattice vectors of the high-symmetry phase. Here, a and b (a^* and b^*) are the basis vectors of the high-symmetry $1T$ phase in real (reciprocal) space, and a and b (q_1 and q_2) are the lattice vectors of CDW structures in real (reciprocal) space.

	2×2	4×4	$2 \times \sqrt{3}$	$4 \times \sqrt{3}$	$\sqrt{7} \times \sqrt{3}$
a'	$2a$	$4a$	$2a$	$4a$	$3a + 2b$
b'	$2b$	$4b$	$-a + 2b$	$-a + b$	$-a + b$
q_1	$\frac{1}{2}a^*$	$\frac{1}{4}a^*$	$\frac{1}{2}a^* + \frac{1}{4}b^*$	$\frac{1}{4}a^* + \frac{1}{8}b^*$	$\frac{1}{5}(a^* + b^*)$
q_2	$\frac{1}{2}b^*$	$\frac{1}{4}a^*$	$\frac{1}{2}b^*$	$\frac{1}{4}b^*$	$\frac{1}{5}(-2a^* + b^*)$

With the improvement in the preparation process, various materials were successfully synthesized in monolayer or few-layer form. The monolayer $1T$-VSe_2 was successfully synthesized, accompanied by various CDW superstructures, such as 2×2, 4×4, $2 \times \sqrt{3}$, $4 \times \sqrt{3}$, and $\sqrt{7} \times \sqrt{3}$ [34–40]. We simulate the various CDW superstructures to find the ground state and further clarify the origin of the multiple CDW order formation. First, we select the lattice vectors as listed in Table I, which are commensurate with the high-symmetry $1T$-VSe_2. Then, we set the displacement of V atoms in the range of 3%–7% considering the related symmetry. Finally, we relax the lattice and atomic positions completely to obtain the final superstructures, as shown in Figs. 3(a)–3(c). Using the relationship of the conversion between the real and reciprocal spaces, we can obtain Q_{CDW} of various CDW superstructures, which are listed in Table I. In order to find the real CDW ground state of monolayer $1T$-VSe_2, we evaluate the various CDW superstructures mentioned above in view of energy. We calculated the energy gain of the CDW formation by $\Delta E = E_{\mathrm{CDW}} - E_{1T}$. Since the various tested unit cell sizes yielded quantitatively similar results, we calculated E_{1T} by using the unit cell of undistorted monolayer $1T$-VSe_2. If ΔE has a negative value, the larger $|\Delta E|$ indicates the more stable system. For different CDW superstructures, we used the k-point meshes with $0.02 \times 2\pi$ Å^{-1} for the sake of comparison. We can see that the $\sqrt{7} \times \sqrt{3}$ cluster has the biggest energy gain from Table II, indicating that the $\sqrt{7} \times \sqrt{3}$ superstructure is the thermodynamically favorable state.

With insight into the origin of the multiple CDW orders in monolayer VSe_2, we further investigate the electron and phonon properties of monolayer $1T$-VSe_2 with the normal phase (undistorted $1T$ structure). The band structure and Fermi surface of monolayer $1T$-VSe_2 are shown in Fig. SII of the Supplemental Material [53]. We evaluate the Fermi-surface nesting of monolayer $1T$-VSe_2 by calculating the

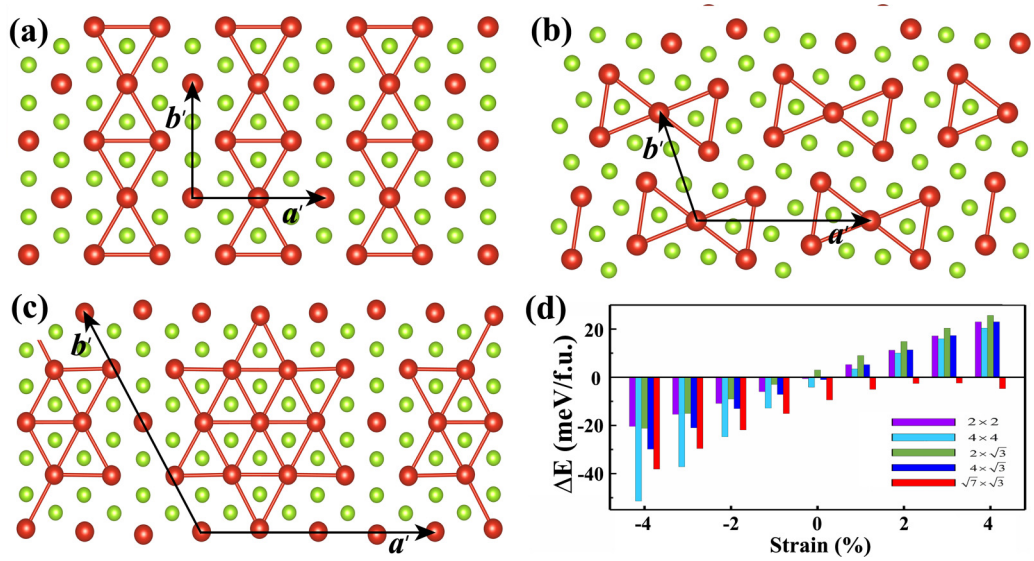

FIG. 3. Superstructures of (a) $2 \times \sqrt{3}$, (b)$\sqrt{7} \times \sqrt{3}$, and (c) 4×4 CDW orders. (d) Evolution of the energy gain of various CDW superstructures under different strains.

electron susceptibility. The calculated χ' and χ'' in the $q_z = 0$ plane are shown in Figs. 4(a) and 4(b). One can see that both the maximum χ' and χ'' are around $Q'_{//} = Q''_{//} = \frac{2}{5}\Gamma M = \frac{1}{5}a^*$. But the $\frac{1}{5}a^*$ wave-vector-related CDW order was never observed in the experiment. Thus, the Fermi-surface nesting cannot account for the CDW formation in monolayer $1T$-VSe_2.

Figure 4(c) shows the phonon dispersion curves of monolayer $1T$-VSe_2. There are two prominent unstable phonon modes indicated by the red arrows. The two softened modes are marked as Q_1 and Q_2, with q vectors of $Q_1 = \frac{1}{2}\Gamma M = \frac{1}{4}a^*$ and $Q_2 = \frac{3}{5}\Gamma K = \frac{1}{5}(a^* + b^*)$. Similar to the previous report by Esters *et al.* [56], we calculated the phonon dispersion with the spin-polarized monolayer $1T$-VSe_2 (see Fig. SIII in the Supplemental Material [53]) and found that the non-spin-polarized calculations can describe the phonon dispersion well to study CDWs. The calculated phonon linewidth of the lowest phonon mode in the $q_z = 0$ plane is shown in Fig. 4(d). The two larger values are around Q_1 and Q_2, consistent with the phonon softened modes. In real space, Q_1 and Q_2 are related to the 4×4 and $\sqrt{7} \times \sqrt{3}$ CDW orders of monolayer $1T$-VSe_2, respectively. Compared with the case of bulk $1T$-VSe_2, the EPC may play an important role in CDW formation of monolayer $1T$-VSe_2.

Considering the experimentally prepared monolayer $1T$-VSe_2 on different substrates, we investigate the effects of in-plane biaxial strain on the multiple CDW orders mentioned above. First, we study the evolution of the energy gain under different strains for various CDW superstructures. When the compressive strain is applied to the CDW superstructures, the energy gain increases rapidly with increasing strain, as shown in Fig. 3(d), which means that the compressive strain benefits various CDW orders. The interesting thing is that when the compressive stress is larger than 2%, the 4×4 CDW superstructure has a larger energy reduction than the $\sqrt{7} \times \sqrt{3}$ CDW superstructure does, indicating that the compressive strain can turn the ground state from the $\sqrt{7} \times \sqrt{3}$ CDW order to the 4×4 one. In contrast, when the tensile strain is applied, the $\sqrt{7} \times \sqrt{3}$ superstructure still has a negative energy gain, implying that the $\sqrt{7} \times \sqrt{3}$ CDW order can survive with tensile strain. In experiments, most of the substrates used (except for Al_2O_3) have smaller lattice parameters

TABLE II. Energy gain of the CDW formation (meV/f.u.) of pristine freestanding monolayer $1T$-VSe_2. The cases of compressive (−4%) and tensile (+4%) strains are also listed here.

	2×2	4×4	$2 \times \sqrt{3}$	$4 \times \sqrt{3}$	$\sqrt{7} \times \sqrt{3}$
−4%	−20.42	−51.42	−21.18	−29.83	−38.13
Pristine	−0.58	−4.14	3.0	−1.01	−9.41
+4%	22.97	20.44	25.67	22.99	−4.73

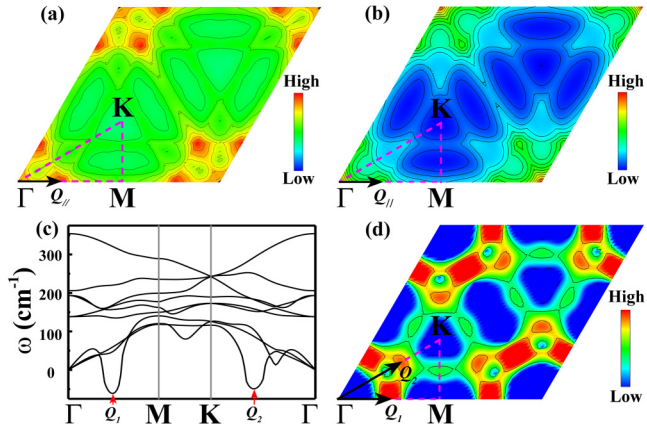

FIG. 4. Cross section of the (a) real and (b) imaginary parts of electron susceptibility of monolayer $1T$-VSe_2 in the $q_z = 0$ plane. (c) Phonon dispersion curves of monolayer $1T$-VSe_2, where Q_1 and Q_2 stand for the two prominent imaginary frequencies. (d) Phonon linewidth of the lowest phonon mode of monolayer $1T$-VSe_2 in the $q_z = 0$ plane.

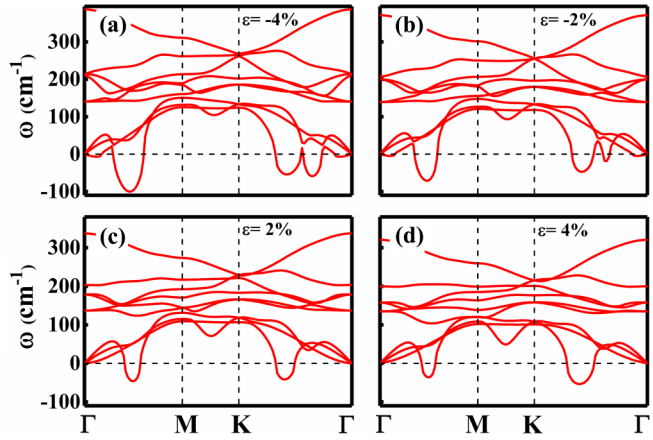

FIG. 5. Phonon dispersion curves of monolayer 1T-VSe_2 under (a) and (b) compressive strain and (c) and (d) tensile strain.

than 1T-VSe_2 [34,35,37–40]. The experimentally observed different CDW orders in monolayer 1T-VSe_2 could be mainly due to the different compressive strains induced by substrates.

Finally, we evaluate the stability of various CDW orders under strain with regard to phonons. Figure 5 shows the calculated phonon dispersion curves of undistorted monolayer 1T-VSe_2 under different strains. It shows that the compressive strain makes the softened mode Q_1 become larger [Figs. 5(a) and 5(b)], implying the enhanced 4×4 CDW order, consistent with the above calculation result of energy gain using CDW superstructure. When the biaxial tensile strain is applied to the system [Figs. 5(c) and 5(d)], the softened mode Q_2, which is related to the $\sqrt{7} \times \sqrt{3}$ CDW order, gradually broadens, while the softened mode Q_1 slightly decreases. In addition, we found that when the tensile strain increases to 6%, the phonon spectrum has a large area of imaginary frequency, indicating the system fully loses stability under larger strain.

IV. CONCLUSIONS

In conclusion, we have theoretically investigated the origin of CDW orders in 1T-VSe_2 and the strain effect of multiple CDW orders. The present results show that both Fermi-surface nesting and electron-phonon coupling account for the $4 \times 4 \times 3$ CDW order in bulk 1T-VSe_2, while the electron-phonon coupling is dominant in the origin of the $\sqrt{7} \times \sqrt{3}$ CDW order of freestanding monolayer 1T-VSe_2. The compressive strain can turn the ground state from the $\sqrt{7} \times \sqrt{3}$ CDW order to the 4×4 CDW order, while the tensile strain can maintain the $\sqrt{7} \times \sqrt{3}$ one. Our results demonstrate the origin of the CDW orders in 1T-VSe_2 and shed some light on understanding the experimental observations of various CDW orders in monolayer 1T-VSe_2.

ACKNOWLEDGMENTS

This work was supported by the National Key R&D Program of China under Contract No. 2016YFA0300404, the National Nature Science Foundation of China under Contracts No. 11774351 and No. 11704001, and the Open Project of State Key Laboratory of Superhard Materials, Jilin University (Grant No. 201902). The calculations were partially performed at the Center for Computational Science, CASHIPS.

[1] K. S. Novoselov, A. K. Geim, S. V. Morozov, D. Jiang, Y. Zhang, S. V. Dubonos, I. V. Grigorieva, and A. A. Firsov, Science **306**, 666 (2004).
[2] C. L. Kane and E. J. Mele, Phys. Rev. Lett. **95**, 226801 (2005).
[3] S. Manzeli, D. Ovchinnikov, D. Pasquier, O. V. Yazyev, and A. Kis, Nat. Rev. Mater. **2**, 17033 (2017).
[4] M. Chhowalla, H. S. Shin, G. Eda, L.-J. Li, K. P. Loh, and H. Zhang, Nat. Chem. **5**, 263 (2013).
[5] J. van Wezel, R. Schuster, A. König, M. Knupfer, J. van den Brink, H. Berger, and B. Büchner, Phys. Rev. Lett. **107**, 176404 (2011).
[6] U. Chatterjee, J. Zhao, M. Iavarone, R. D. Capua, J. P. Castellan, G. Karapetrov, C. D. Malliakas, M. G. Kanatzidis, H. Claus, J. P. C. Ruff, F. Weber, J. Van Wezel, J. C. Campuzano, R. Osborn, M. Randeria, N. Trivedi, M. R. Norman, and S. Rosenkranz, Nat. Commun. **6**, 6313 (2015).
[7] F. Flicker, and J. van Wezel, Nat. Commun. **6**, 7034 (2015).
[8] D. Mihailovic, D. Dvorsek, V. V. Kabanov, J. Demsar, L. Forró, and H. Berger, Appl. Phys. Lett. **80**, 871 (2002).
[9] J. Khan, C. M. Nolen, D. Teweldebrhan, D. Wickramaratne, R. K. Lake, and A. A. Balandin, Appl. Phys. Lett. **100**, 043109 (2012).
[10] N. Ogawa and K. Miyano, Appl. Phys. Lett. **80**, 3225 (2002).
[11] P. Goli, J. Khan, D. Wickramaratne, R. K. Lake, and A. A. Balandin, Nano Lett. **12**, 5941 (2012).
[12] C. Battaglia, H. Cercellier, F. Clerc, L. Despont, M. G. Garnier, C. Koitzsch, P. Aebi, H. Berger, L. Forró, and C. Ambrosch-Draxl, Phys. Rev. B **72**, 195114 (2005).
[13] H. Myron and A. J. Freeman, Phys. Rev. B **11**, 2735 (1975).
[14] M. D. Johannes and I. I. Mazin, Phys. Rev. B **77**, 165135 (2008).
[15] F. Weber, S. Rosenkranz, J.-P. Castellan, R. Osborn, G. Karapetrov, R. Hott, R. Heid, K.-P. Bohnen, and A. Alatas, Phys. Rev. Lett. **107**, 266401 (2011).
[16] M. Calandra and F. Mauri, Phys. Rev. Lett. **106**, 196406 (2011).
[17] A. Y. Liu, Phys. Rev. B **79**, 220515(R) (2009).
[18] C. Monney, C. Battaglia, H. Cercellier, P. Aebi, and H. Beck, Phys. Rev. Lett. **106**, 106404 (2011).
[19] C. Chen, B. Singh, H. Lin, and V. M. Pereira, Phys. Rev. Lett. **121**, 226602 (2018).
[20] T. E. Kidd, T. Miller, M. Y. Chou, and T.-C. Chiang, Phys. Rev. Lett. **88**, 226402 (2002).
[21] K. Wijayaratne, J. Zhao, C. Malliakas, D. Y. Chung, M. G. Kanatzidisbc, and U. Chatterjee, J. Mater. Chem. C **5**, 11310 (2017).
[22] C. M. Varma and W. Weber, Phys. Rev. Lett. **39**, 1094 (1977).
[23] N. Doran, J. Phys. C **11**, L959 (1978).
[24] J. Henke, F. Flicker, J. Laverock, and J. van Wezel, arXiv:1911.11112.
[25] W. Kohn, Phys. Rev. Lett. **19**, 439 (1967).
[26] D. Jérome, T. Rice, and W. Kohn, Phys. Rev. **158**, 462 (1967).

[27] B. Halperin, and T. Rice, Solid State Phys. **21**, 115 (1968).
[28] B. Halperin and T. Rice, Rev. Mod. Phys. **40**, 755 (1968).
[29] A. Kogar, M. S. Rak, S. Vig, A. A. Husain, F. Flicker, Y. I. Joe, L. Venema, G. J. MacDougall, T. C. Chiang, and E. Fradkin, Science **358**, 1314 (2017).
[30] H. Cercellier, C. Monney, F. Clerc, C. Battaglia, L. Despont, M. G. Garnier, H. Beck, P. Aebi, L. Patthey, H. Berger, and L. Forró, Phys. Rev. Lett. **99**, 146403 (2007).
[31] J. van Wezel, P. Nahai-Williamson, and S. S. Saxena, Phys. Rev. B **81**, 165109 (2010).
[32] D. J. Eaglesham, R. L. Withers, and D. M. Bird, J. Phys. C **19**, 359 (1986).
[33] K. Terashima, T. Sato, H. Komatsu, T. Takahashi, N. Maeda, and K. Hayashi, Phys. Rev. B **68**, 155108 (2003).
[34] M. Bonilla, S. Kolekar, Y. Ma, H. C. Diaz, V. Kalappattil, R. Das, T. Eggers, H. R. Gutierrez, M.-H. Phan, and M. Batzill, Nat. Nanotechnol. **13**, 289 (2018).
[35] P. Chen, W. W. Pai, Y.-H. Chan, V. Madhavan, M.-Y. Chou, S.-K. Mo, A.-V. Fedorov, and T.-C. Chiang, Phys. Rev. Lett. **121**, 196402 (2018).
[36] A. O. Fumege, M. Gobbi, P. Dreher, W. Wan, C. González-Orellana, M. Peña-Díaz, C. Rogero, J. Herrero-Martín, P. Gargiani, M. Ilin, M. M. Ugeda, V. Pardo, and S. Blanco-Canosa, J. Phys. Chem. C **123**, 27802 (2019).
[37] J. Feng, D. Biswas, A. Rajan, M. D. Watson, F. Mazzola, O. J. Clark, K. Underwood, I. Marković, M. Mclaren, A. Hunter, D. M. Burn, L. B. Duffy, S. Barua, G. Balakrishnan, F. Bertran, P. L. Fèvre, T. K. Kim, G. van der Laan, T. Hesjedal, P. Wahl, and P. D. C. King, Nano Lett. **18**, 4493 (2018).
[38] W. Jolie, T. Knispel, N. Ehlen, K. Nikonov, C. Busse, A. Grüneis, and T. Michely, Phys. Rev. B **99**, 115417 (2019).
[39] G. Duvjir, B. K. Choi, I. Jang, S. Ulstrup, S. Kang, T. T. Ly, S. Kim, Y. H. Choi, C. Jozwiak, A. Bostwick, E. Rotenberg, J.-G. Park, R. Sankar, K.-S. Kim, J. Kim, and Y. J. Chang, Nano Lett. **18**, 5432 (2018).
[40] D. Zhang, J. Ha, H. Baek, Y.-H. Chan, F. D. Natterer, A. F. Myers, J. D. Schumacher, W. G. Cullen, A. V. Davydov, Y. Kuk, M. Y. Chou, N. B. Zhitenev, and J. A. Stroscio, Phys. Rev. Mater. **1**, 024005 (2017).
[41] X. Wang, H. Liu, J. Wu, J. Lin, W. He, H. Wang, X. Shi, K. Suenaga, and L. Xie, Adv. Mater. **30**, 1800074 (2018).
[42] H. Ryu, Y. Chen, H. Kim, H.-Z. Tsai, S. Tang, J. Jiang, F. Liou, S. Kahn, C. Jia, and A. A. Omrani, Nano lett. **18**, 689 (2018).
[43] O. R. Albertini, R. Zhao, R. L. McCann, S. Feng, M. Terrones, J. K. Freericks, J. A. Robinson, and A. Y. Liu, Phys. Rev. B **93**, 214109 (2016).
[44] J. Shi, X. Chen, L. Zhao, Y. Gong, M. Hong, Y. Huan, Z. Zhang, P. Yang, Y. Li, and Q. Zhang, Adv. Mater. **30**, 1804616 (2018).
[45] J.-P. Peng, J.-Q. Guan, H.-M. Zhang, C.-L. Song, L. Wang, K. He, Q.-K. Xue, and X.-C. Ma, Phys. Rev. B **91**, 121113(R) (2015).
[46] P. Chen, Y.-H. Chan, X.-Y. Fang, Y. Zhang, M.-Y. Chou, S.-K. Mo, Z. Hussain, A.-V. Fedorov, and T.-C. Chiang, Nat. Commun. **6**, 1 (2015).
[47] M. J. Wei, W. J. Lu, R. C. Xiao, H. Y. Lv, P. Tong, W. H. Song, and Y. P. Sun, Phys. Rev. B **96**, 165404 (2017).
[48] G. Paolo, B. Stefano, B. Nicola, C. Matteo, C. Roberto, C. Carlo, C. Davide, L. C. Guido, C. Matteo, D. Ismaila, C. AndreaDal, G. Stefano de, F. Stefano, F. Guido, G. Ralph, G. Uwe, G. Christos, K. Anton, L. Michele, M.-S. Layla, M. Nicola, M. Francesco, M. Riccardo, P. Stefano, P. Alfredo, P. Lorenzo, S. Carlo, S. Sandro, S. Gabriele, P. S. Ari, S. Alexander, U. Paolo, and M. W. Renata, J. Phys.: Condens. Matter **21**, 395502 (2009).
[49] D. Vanderbilt, Phys. Rev. B **41**, 7892 (1990).
[50] J. P. Perdew, K. Burke, and M. Ernzerhof, Phys. Rev. Lett. **77**, 3865 (1996).
[51] S. Grimme, J. Comput. Chem. **27**, 1787 (2006).
[52] S. Baroni, S. De Gironcoli, A. Dal Corso, and P. Giannozzi, Rev. Mod. Phys. **73**, 515 (2001).
[53] See Supplemental Material at http://link.aps.org/supplemental/10.1103/PhysRevB.101.235405 for electronic structures of bulk and monolayer 1T-VSe_2 and phonon dispersion curves of spin-polarized 1T-VSe_2.
[54] V. N. Strocov, M. Shi, M. Kobayashi, C. Monney, X. Wang, J. Krempasky, T. Schmitt, L. Patthey, H. Berger, and P. Blaha, Phys. Rev. Lett. **109**, 086401 (2012).
[55] F. Clerc, C. Battaglia, M. Bovet, L. Despont, C. Monney, H. Cercellier, M. G. Garnier, P. Aebi, H. Berger, and L. Forró, Phys. Rev. B **74**, 155114 (2006).
[56] M. Esters, R. G. Hennig, and D. C. Johnson, Phys. Rev. B **96**, 235147 (2017).